Combustion Theory and Modelling, 2021
Vol. 25, No. 5, 940–967, https://doi.org/10.1080/13647830.2021.1962981

Numerical methodology for spontaneous wrinkling of centrally ignited premixed flames – linear theory

Shikhar Mohan * and Moshe Matalon

Department of Mechanical Science and Engineering, University of Illinois at Urbana-Champaign, Urbana, IL, USA

(*Received 30 September 2020; accepted 19 July 2021*)

An improved embedded-manifold/Navier–Stokes numerical methodology is developed to simulate the propagation of premixed flames within the context of the hydrodynamic theory. The method is computationally tractable, permitting calculations to not only be extended to larger physical domains but also to span a broader parametric space of physicochemical parameters. The focus of this paper is to examine the susceptibility of centrally ignited, freely propagating and outwardly expanding circular flames to small amplitude disturbances and observe the flame's development through the onset of the hydrodynamic instability. The numerical simulations, validated by a linear stability analysis, show that for mixtures with Lewis numbers above criticality, thermo-diffusive effects exert stabilising influences which dominate at small flame radii, initially suppressing the growth of all disturbances. Consistent with the linear theory, simulations show the flame initially remaining stable and demonstrate the existence of a particular mode which is the first to grow. This mode is said to dictate the cellular pattern observed experimentally at the onset of instability. The variation in critical flame radius with respect to the Markstein length and thermal expansion coefficients are in quantitative agreement with these analytical results.

Keywords: Darrieus–Landau instability; expanding flames; spontaneous wrinkling; flame stretch; hydrodynamic theory

1. Introduction

Large-scale premixed flames are always susceptible to hydrodynamic instabilities. These instabilities are known to partially contribute to the cellular appearance of spherical flames in lean methane-air, and hydrogen-air mixtures and almost wholly in lean mixtures of heavier hydrocarbons and rich hydrogen-air mixtures. The presence of the hydrodynamic instability was originally identified in the pioneering works of Darrieus [1] and Landau [2], and is referred to nowadays as the Darrieus–Landau (DL) instability. In the aforementioned works, the flame was idealised as a structureless surface, separating burnt gases from unburnt mixture, and propagating at constant speed; it was shown that planar deflagrations were unconditionally unstable. Recognising that this result was not valid for disturbances with wavelength comparable to the flame thickness, Markstein [3] introduced a correction to the flame speed proportional to the local flame-front's curvature, albeit as a phenomenological refinement, illustrating that diffusive processes may exert stabilising influences on the shorter wavelength disturbances. However, the functional dependence between this

*Corresponding author. Email: smmohan2@illinois.edu

parameter, later becoming known as the Markstein length, to physicochemical parameters of the system remained unclear.

The stability of planar flames was clarified by the more rigorous asymptotic studies of Pelce & Clavin [4], Frankel & Sivashinsky [5] and Matalon & Matkowsky [6], which accounted for diffusion processes occurring inside the flame zone using a multi-scale approach. The flame speed in this systematic approach was found to depend on the local flame stretch rate; this combined the effects of curvature and hydrodynamic strain-rate, and the revised stability analysis showed conclusively that for planar flames diffusion effects have a stabilising influence on short wavelength disturbances when the effective Lewis number of the mixture is above a critical value, slightly below one. In addition, these studies related the previously ad-hoc Markstein length to meaningful physicochemical properties of the mixture. Whilst the conclusions drawn by these three independent studies were identical, the mathematical approaches were different. Pelce & Clavin and Frankel & Sivashinsky first linearised the governing equations about a planar flame solution, and then used a multi-scale approach to incorporate the effects of diffusion with the perturbed equations. Instead, Matalon & Matkowsky derived a generalised framework for treating flames of arbitrary shape in arbitrary flow fields to examine the stability of planar flames. This more generalised formulation, referred to below as the hydrodynamic theory, was subsequently cast in a coordinate-free form [7] which allowed the dynamics of flames other than those in a planar configuration to be studied, such as the stability of centrally ignited and outwardly growing flames; the focus of the present work.

The stability of spherically expanding flames was first examined by Istratov & Librovich [8] using a Markstein model. Their results suggested that, for some range of Markstein lengths, the initial phase of flame propagation is associated with a period of decay for all disturbances, and that the onset of instability corresponds to a critical Reynolds number (based on the flame radius). This critical Reynolds number was seen to vary as a function of the thermal expansion ratio. Using the hydrodynamic formulation, Bechtold & Matalon [9] re-examined this stability problem and derived stability criteria for freely expanding spherical flames that accounted for both, realistic gas expansion as well as the influences of molecular and thermal diffusion occurring inside the flame zone. This analysis was later updated by Addabbo et al. [10] to incorporate effects due to stoichiometry and more realistic temperature-dependent transport coefficients. These studies conclusively showed that when the effective Lewis number of the mixture was above criticality, the expanding flame was initially stable to small amplitude disturbances before growing once the flame had achieved a critical radius. Visually, this corresponds to a flame that initially propagates smoothly until reaching a certain size beyond which the stabilising influences exerted by molecular/thermal diffusion are diminished resulting in a corrugated front. The effective Lewis number was found to be a stoichiometry-weighted average of the individual Lewis numbers of the fuel and oxidiser, with the deficient component in the mixture weighting more heavily [11]. Accordingly, cellular flames are observed in mixtures where the deficient component is less mobile (or heavier), such as lean hydrocarbon-air or rich hydrogen-air mixtures. The linear stability analysis also confirmed the existence of a critical wavenumber perturbation that would be the first to grow such that, when exceeding the critical radius, the flame becomes spontaneously covered by a large number of cells, and provided estimates of the upper and lower bounds of the cell sizes.

These predictions are consistent with the observations made by Groff [12] in an early experiment on confined spherical flames in lean propane-air mixtures where cells with distinct polyhedral structures became noticeable once the flame had reached a critical size.

Since the light-reactant was in excess and thus thermo-diffusive effects were stabilising, he concluded that the irregularity in flame shape was largely due to the DL instability. It was further noted that the point of transition to cellularity was strongly affected by the thermal expansion parameter. The onset of cellularity in flames with radii significantly larger than the laminar flame thickness, and the dependence on mixture composition and pressure level predicted in the theory of Bechtold & Matalon [9, 10] were later confirmed in a series of experiments [13–18]. The experimental work demonstrated that the amplification of hydrodynamic disturbances by thermal expansion morphed the flame topology into a fractal-like pattern and led to self-acceleration and enhancement in propagation speed.

The overall objective of this work is to examine the evolution of outwardly propagating flames numerically using the hydrodynamic theory which, unlike fully resolved, direct numerical simulations of the complete equations, is computationally efficient. The calculations can thereby be extended to adequately large domains such that the growth of boundary effects are suppressed and prevented from contaminating the solution. Equally importantly, it permits a systematic examination of intricate flame dynamics for a wider range of parameters, of which there are two namely: the unburnt-to-burnt density ratio, which is proportional to the heat released by the chemical reactions, and the Markstein length that lumps the reactive and diffusive properties of the mixture, the equivalence ratio and the system's pressure level. The hydrodynamic theory is particularly applicable as the flame becomes increasingly thin the larger it grows, especially in the regime where self-acceleration and self-turbulisation become distinctly observable. To this end, a numerical methodology, one adept at reproducing the fine-grained structures frequently reported in outwardly growing flames, based on the hydrodynamic theory is developed; it is an improvement on the hybrid level-set/Navier–Stokes scheme proposed by Rastigejev & Matalon [19], Creta & Matalon [20] and used in subsequent works [21, 22]. As a first step in its implementation, the early phase of propagation of outwardly growing circular flames is examined. This includes the linear regime when the amplitude of disturbances remains small and evolves at a rate comparable to the overall flame propagation velocity, and the early nonlinear development that extends the flame evolution to a regime beyond what may be considered as the "onset of instability". Analytical expressions for the growth rate of arbitrary modes and key conditions (flame radii and critical wavenumber that determine stability) are derived using a linear stability analysis, similar to that of Bechtold & Matalon [9] for spherically expanding flames, as functions of physically meaningful parameters. These theoretical results not only provide insight into the initial transient behaviour of the flame, but serve as a measure of numerical fidelity when extending the numerical methodology to the highly nonlinear regime, which will be the subject of a subsequent article.

2. The hydrodynamic model

The hydrodynamic theory is based on a multi-scale approach that exploits the various length scales associated with the combustion process. Typically, the diffusion length characterising the flame thickness, and defined as $l_f = \mathcal{D}_{th}/S_L$ where $\mathcal{D}_{th}$ is the thermal diffusivity of the mixture and S_L the laminar flame speed, is much smaller than the length L characterising the hydrodynamic field, such that $\delta \equiv l_f/L \ll 1$. As a consequence, the flame can be treated as a thin layer where transport processes dominate, whilst the chemical reactions due to the large activation energy are confined to a yet thinner layer within this

zone. Therefore, when viewed on the much larger hydrodynamic length-scale, the flame devolves into a moving interface, described by $\psi(\mathbf{x}, t) = 0$, that separates the burnt products in the region $\psi > 0$ from the unburnt mixture in the region $\psi < 0$; here $\mathbf{x}$ is the vector position and t the time variable. The flow field is obtained by integrating the Euler equations with $\mathcal{O}(\delta)$ viscous corrections on either side of the flame and imposing mass and momentum conservation across the interface in the form of modified Rankine–Hugoniot jump conditions. The flame speed, defined as the propagation speed relative to the unburnt gas, is the laminar flame speed S_L with an $\mathcal{O}(\delta)$ correction that accounts for the stretch rate and is modulated by a Markstein length that mimics the diffusion and chemical reaction processes occurring inside the flame zone. Further details of the hydrodynamic model can be found in [6, 7, 11].

In the following, a Markstein-type model is adopted, retaining for simplicity the $\mathcal{O}(\delta)$ corrections only to the flame speed relation, which enables a comparison with numerical simulations of the hydrodynamic model developed so far for such conditions. For planar flames, this simplification has been shown to slightly shift the critical Lewis number above which diffusion effects have stabilising influences on the flame dynamics, but otherwise provides the same stability results as predicted by the more rigorous asymptotic study [23]. The mathematical problem thus consists of

$$\boldsymbol{\nabla} \cdot \mathbf{v} = 0 \tag{1}$$

$$\rho \left(\frac{\partial \mathbf{v}}{\partial t} + (\mathbf{v} \cdot \boldsymbol{\nabla})\mathbf{v} \right) = -\boldsymbol{\nabla} p \tag{2}$$

where $\mathbf{v}$ is the velocity, p the pressure and ρ the density of the mixture given by

$$\rho = \begin{cases} \rho_u & \text{for } \psi(\mathbf{x}, t) < 0 \\ \rho_b & \text{for } \psi(\mathbf{x}, t) > 0 \end{cases}, \tag{3}$$

where the subscripts u and b stand for "unburnt" and "burnt", respectively. These equations are to be solved on either side of the flame subject to the Rankine–Hugoniot (RH) relations

$$\begin{aligned} &[\![\rho(\mathbf{v} \cdot \mathbf{n} - V_f)]\!] = 0 \\ &[\![\mathbf{n} \times (\mathbf{v} \times \mathbf{n})]\!] = 0 \\ &[\![p + \rho(\mathbf{v} \cdot \mathbf{n})(\mathbf{v} \cdot \mathbf{n} - V_f)]\!] = 0 \end{aligned} \tag{4}$$

where $[\![\cdot]\!]$ denotes the jump operator, and

$$\mathbf{n} = \frac{\boldsymbol{\nabla}\psi}{|\boldsymbol{\nabla}\psi|}, \quad V_f = -\frac{1}{|\boldsymbol{\nabla}\psi|}\frac{\partial \psi}{\partial t}$$

are, respectively, the unit vector normal to the flame surface pointing towards the burnt gas region, and the propagation speed (measured with respect to a fixed coordinate system). The flame speed, defined as the propagation speed relative to the incoming flow, namely $S_f \equiv \mathbf{v}^* \cdot \mathbf{n} - V_f$ where $\mathbf{v}^*$ is the gas velocity evaluated at the flame front on its unburnt side, is given by

$$S_f = S_L - \mathcal{L}\,\mathbb{K} \tag{5}$$

where $\mathbb{K}$ is the flame stretch rate given by

$$\mathbb{K} = -V_f \kappa - \mathbf{n}\cdot\boldsymbol{\nabla}\times(\mathbf{v}^*\times\mathbf{n}) \tag{6}$$

with $\kappa = -\boldsymbol{\nabla}\cdot\mathbf{n}$ the local curvature of the flame front [24]. The second term on the right-hand side of (6) corresponds to the surface extension resulting from velocity gradients along the flame surface and may be expressed as $-\boldsymbol{\nabla}_s\cdot\mathbf{v}_s^*$, where $\boldsymbol{\nabla}_s$ is the surface gradient and $\mathbf{v}_s^*$ the component of the velocity vector tangent to the flame surface. Since $\mathbf{v}_s^*$ is continuous across the flame, the stretch rate is uniquely defined on the interface, regardless of whether evaluated on its unburnt or burnt side. The proportionality coefficient $\mathcal{L}$ in the flame speed-flame stretch relation (6) is the Markstein length, an expression for which can be found in [11]. Finally, it is noted that the hydrodynamic model is valid only for $\mathcal{L} > 0$, which constitutes the range of interest of the present study.

It is often stated that flame stretch may be expressed as a combination of curvature and strain, which is correct in the asymptotic limit considered in the hydrodynamic model. Indeed, expanding the right-hand side of (6) and using the leading order approximation $S_f \sim S_L$, one finds that

$$\mathbb{K} = S_L\kappa - \mathbf{n}\cdot\mathbf{E}\cdot\mathbf{n} + \boldsymbol{\nabla}\cdot\mathbf{v}$$

where $\mathbf{E}$ is the strain-rate tensor, which reduces to

$$\mathbb{K} = S_L\kappa + K_S \quad K_S = -\mathbf{n}\cdot\mathbf{E}\cdot\mathbf{n} \tag{7}$$

when $\boldsymbol{\nabla}\cdot\mathbf{v} = 0$. Else, in computations that resolve the flame structure, the use of Equation (7) underestimates the stretch rate, and the reported value of stretch depends on the representative surface within the flow field that is selected to represent the "flame surface". An unambiguous and unique value consistent with the hydrodynamic theory results if the additional constraint $\boldsymbol{\nabla}\cdot\mathbf{v} = 0$ is imposed when evaluating the stretch rate, as suggested in [25].

3. Numerical methodology

The nonlinear free-boundary hydrodynamic problem is numerically implemented as a combination of two modules, as originally proposed by Rastigeyev and Matalon [26]. The first involves embedding the flame interface (curves in two-dimensional flows) as a level set of an associated Cartesian scalar field $\psi(\mathbf{x}, t)$. A *continuum* approach is preferred wherein discontinuities in density are smeared over a few computational grid cells. The flame is therefore represented by a mollified Heaviside function of the form

$$\rho(\psi) = \rho_u + \frac{1}{2}(\rho_u - \rho_b)\left(1 + \tanh\frac{\psi}{h}\right) \tag{8}$$

where h represents a numerical flame thickness and is taken to be an integer multiple of the uniform grid spacing Δx. The flame interface is identified as the zeroth level-set (i.e. $\psi = 0$) of the scalar field. Along the front, the density is a constant $\frac{1}{2}(\rho_u + \rho_b)$ and varies normal to the flame surface taking values ρ_u and ρ_b on the unburnt and burnt sides, respectively. Although by adopting a continuum approach an artificial flame thickness h is introduced, the equations for the velocity and pressure fields can be integrated in a single sweep over the entire domain in contrast to discontinuous approaches. The integration is

accomplished by means of a modified version of IAMR [27] which is a time-dependent, low Mach number, incompressible Navier–Stokes solver. The Navier–Stokes equations with a sufficiently large Reynolds number were used in lieu of the Euler Equations (1) and (2), in order to add a small degree of dissipation to the system. The two modules are linked through the introduction of a singular source term into Equation (1), namely

$$\nabla \cdot \mathbf{v} = \rho_u S_f \frac{\partial}{\partial n}\left(\frac{1}{\rho}\right) \tag{9}$$

which accounts for the effects of gas expansion on the flow field, and through the flow speed dependence on flame stretch. As $h \to 0$, the distribution (8) approaches the piecewise constant function (3) and, when integrating the governing equations with the source term (9), the RH relations are recovered.

The definition of the propagation speed V_f is recast into the level-set equation

$$\frac{\partial \psi}{\partial t} + V_f |\nabla \psi| = 0 \tag{10}$$

used to update the scalar field $\psi(\mathbf{x}, t)$ and, consequently, the density field. The discretisation of the term $V_f|\nabla\psi| = V_f(\psi_x{}^2 + \psi_y{}^2)^{1/2}$ is handled by a Hamilton–Jacobi WENO procedure. Approximations to the left and right-sided derivatives of ψ_x (ψ_x^- and ψ_x^+, respectively), and similarly of ψ_y, are calculated using fifth-order WENO schemes [28]. An upwinding procedure described by Fedkiw et al. [29] based on modifications to Godunov's method is then used. The level-set field ψ is advanced in time using a second-order Total-Variation Diminishing (TVD) Runge–Kutta scheme.

The quantities V_f, S_f and $\mathbb{K}$ (including κ and K_S) are strictly defined on the flame interface whereas the level-set field evolves on a fixed Cartesian grid. To reconcile between the two meshes, a high-order geometrical *closest point method* [30, 31] is used to propagate surface data in a direction normal to the local flame surface onto the Cartesian grid. The method closely follows the implementation described by Saye [32] and is presented briefly here. Initially, a sweep of the domain is performed at the start of each iteration to identify "irregular cells". A grid cell is classified as irregular if it contains a portion of the interface i.e., grid cells at which the scalar ψ changes signs at any one of its vertices. At each irregular cell, a fifth-order polynomial approximation $p(\mathbf{x})$ of ψ between grid points is constructed using a stencil of 24 grid points in two-dimensions and 88 grid points in three-dimensions. The interface is then sampled using the constructed polynomial approximations by "projecting" initial guess values onto the zero level set for each irregular cell. The irregular cells are divided into smaller sub-cells, and the centres of each sub-cell form the set of initial guess values. The following equation is then solved iteratively

$$\mathbf{x}_{i+1} = \mathbf{x}_i - \frac{p(\mathbf{x}_i)\nabla p(\mathbf{x}_i)}{|\nabla p(\mathbf{x}_i)|^2}$$

to project the guess values onto the zeroth level set of the polynomial $p(\mathbf{x})$ until the convergence criterion

$$|x_{i+1} - x_i| \; < 0.01\sqrt{n_{sc}}\,\Delta x$$

is met, where n_{sc} denotes the number of sub-cells created. The outcome of this sampling procedure is a set of scattered points $\mathcal{S}$ that approximate the flame interface along with their associated interpolants.

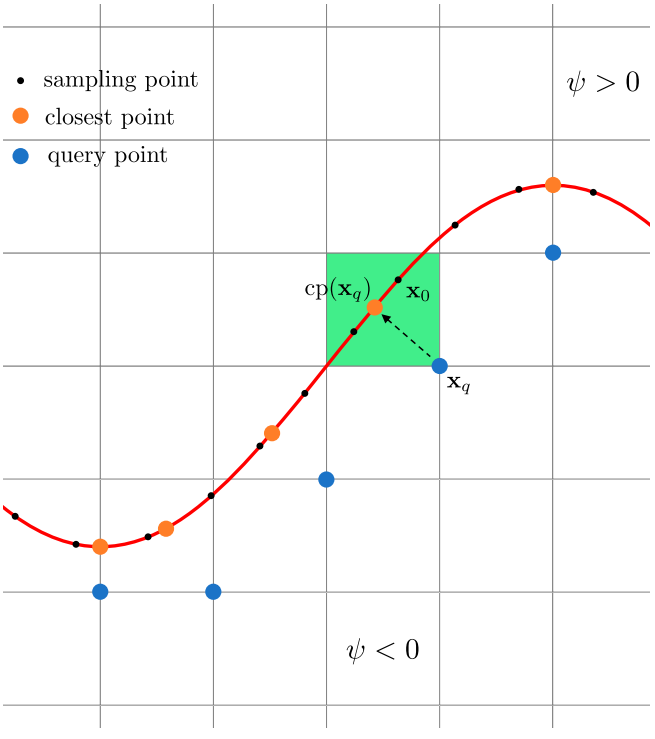

Figure 1. The mapping between a query point $\mathbf{x}_q$, its (perpendicular) closest point projection onto the zeroth level set curve $\text{cp}(\mathbf{x_q})$ and the sampling point x_0 whose associated polynomial is used to describe the local topology (colour online).

For an arbitrary query point $\mathbf{x}_q$ the closest point on $\psi = 0$ is determined by first locating $\mathbf{x}_0$, which is the closest point in the set $\mathcal{S}$ to $\mathbf{x}_q$. This "nearest neighbour" search problem is optimally solved by constructing a k-d tree. Next, the closest point $\text{cp}(\mathbf{x}_q)$ to $\mathbf{x}_q$, which lies on the zero level set of $p(\mathbf{x})$ associated to $\mathbf{x}_0$ is identified; see Figure 1. This step requires the solution to a minimum distance optimisation problem, which can be accomplished by minimising the square distance from the query point $\mathbf{x}_q$ to a point $\mathbf{x}$, subject to the constraint that $\mathbf{x}$ be on the zeroth level-set of the polynomial $p(\mathbf{x})$. This step can be implemented using the method of Lagrange multipliers. The outcome of this procedure is a mapping that links each query point $\mathbf{x}_q$ to the corresponding closest point on the flame surface, i.e. $\text{cp}(\mathbf{x}_q)$. Once interfacial quantities are known at these Lagrangian mesh points, they can be extended back onto the Cartesian grid points. A common method for extending a function ξ defined on the interface is to make it constant along characteristics of the distance function, i.e. $f_{\text{ext}}(\mathbf{x}) = f(\text{cp}(\mathbf{x}))$.

To minimise computational cost, a mask is created around the flame surface such that all grid points that lie within a distance $BW_2\,\Delta x$ from the set of points in $\mathcal{S}$, with BW_2 an integer, are tagged. Interfacial quantities are extended only in this banded region. The cost of the closest point extension, however, is directly proportional to the number of closest point queries made, which increases significantly if this high-order approximation is used throughout the entire banded region. To further minimise the cost, a secondary sub-mask is created which tags grid cells within a radius of $BW_1\,\Delta x$ of the interface, with integer

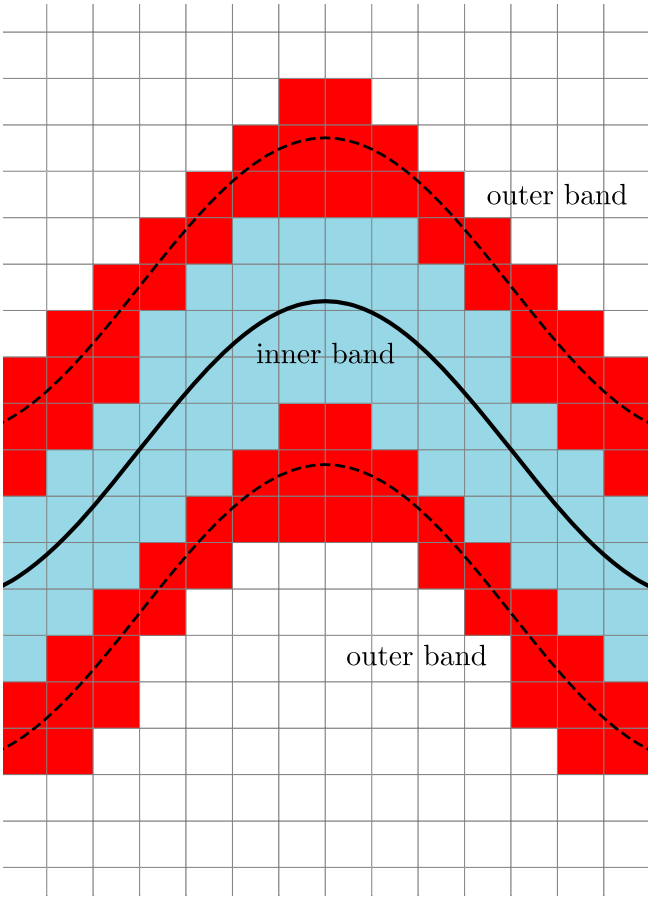

Figure 2. Dual masking; the flame interface is enclosed by two bands where the inner band uses the more accurate closest point extension methodology while the outer uses a pseudo-time PDE-based approach in the interest of minimising computational time (colour online).

$BW_1 < BW_2$. Interfacial quantities are extended using the closest point method only within the inner band; a less accurate, but faster pseudo-time PDE-based approach is used to populate mesh points in the outer band, as discussed below. Figure 2 illustrates the concept of banding with $BW_1 = 2$ and $BW_2 = 4$.

The polynomial representations constructed are also used to evaluate the surface normal $\mathbf{n}$ and mean curvature κ. The normal $\mathbf{n}$ and its derivatives at a point y on the interface are evaluated as follows

$$\mathbf{n}(y) = \left.\frac{\nabla\psi}{|\nabla\psi|}\right|_y,$$

$$\nabla\mathbf{n}(y) = \left.\frac{1}{|\nabla\psi|}(\mathbf{I} - \mathbf{n}\mathbf{n}^{\mathrm{T}})\, D^2\psi\, (\mathbf{I} - \mathbf{n}\mathbf{n}^{\mathrm{T}})\right|_y,$$

where $\mathbf{I}$ is a unitary matrix and $D^2\psi$ is the Hessian matrix, whilst $\kappa(y) = \mathrm{tr}(\nabla\mathbf{n})(y)$. The switch to this approach from a finite differences based approach used previously

became necessary owing to the increased susceptibility of circular and spherical flames to numerical noise that often distorts curvature computations. These inaccuracies in curvature lead to irregularities in curvature profiles along the flame surface and thus erroneous growth-rate profile predictions.

To compute velocity gradients along the flame surface, a stable interpolation technique based on the translative properties of the Dirac delta function coupled together with the RH conditions is used. Since the mass flux normal to the flame surface, $\dot{m} = \rho(\mathbf{v}\cdot\mathbf{n} - V_f) = \rho S_f$, is continuous across the flame, the integration of $\dot{m}\,\delta(n)$ across the entire domain, where n represents the normal distance from $\psi = 0$ towards the burnt gas, yields

$$\mathbf{v}^*\cdot\mathbf{n} = \frac{2}{\rho_b+\rho_u}\int \rho\,(\mathbf{v}\cdot\mathbf{n})\,\delta(n)\,\mathrm{d}n + \frac{\rho_b-\rho_u}{\rho_b+\rho_u}S_f. \tag{11}$$

The tangential velocity component does not experience a jump, so that a similar integration, leads to

$$\mathbf{n}\times\left(\mathbf{v}^*\times\mathbf{n}\right) = \int\left[\mathbf{n}\times(\mathbf{v}\times\mathbf{n})\right]\delta(n)\,\mathrm{d}n\,. \tag{12}$$

In the above equations, it must be emphasised that $\mathbf{n}$ represents the unit normal vector to the flame surface and not the local level set field. Utilizing a normal to the local level set field was found to negatively impact well-known predictions, such as the onset of instability of a planar flame. The gas velocity at the interpolation points, shown in green on Figure 3, are evaluated using a WENO interpolation (described in [31]). The collocation points are straightforward to construct once the direction of the normal is known. This approach is a modified version of the method proposed in [26], where the integration in (11)–(12) was performed in a two- or three-dimensional box formed by a number of cells of the Cartesian grid. Although the results are not affected by this choice when the flame surface is weakly curved, the one-dimensional integration is preferred when the flame becomes sufficiently corrugated. The stretch rate may be evaluated from the relation $\mathbb{K} = S_L\kappa + K_S$, with the straining component determined from $K_S = \partial v_n/\partial n$

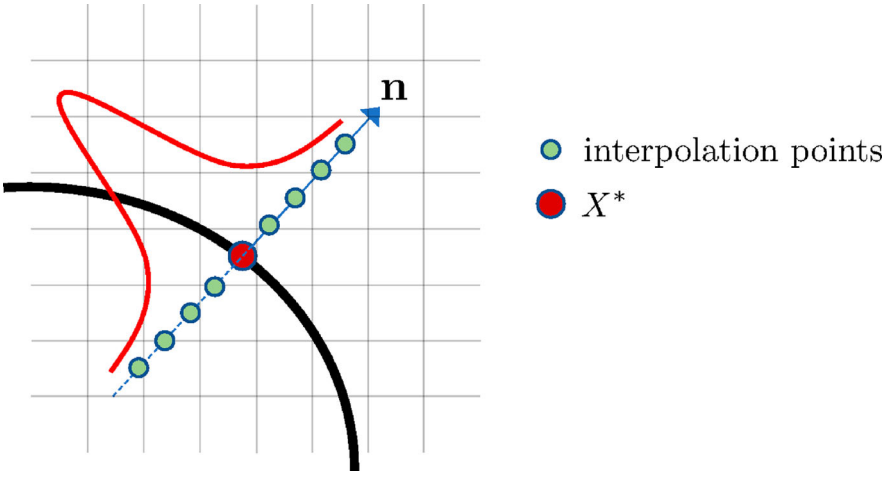

Figure 3. Evaluation of the gas velocity at a Lagrangian point (marked in red) on the flame interface by performing a one-dimensional integration along the normal with respect to a delta function (red curve) (colour online).

evaluated at the interface; here $v_n = \mathbf{v} \cdot \mathbf{n}$ is the normal component of the velocity vector. The introduction of a numerical flame thickness, however, necessitates imposing the constraint $\nabla \cdot \mathbf{v} = 0$, as discussed above. Alternatively, the stretch rate $\mathbb{K}$ may be evaluated directly from (6) as attempted in [22]; in this regard, the polynomial approximation of the flame surface of the closest point method provides a more accurate way of computing the surface gradient.

The propagation speed V_f along the interface is evaluated from the definition of S_f in conjunction with Equation (5), namely

$$V_f = \mathbf{v}^* \cdot \mathbf{n} - (S_L - \mathcal{L}\mathbb{K}) \,. \tag{13}$$

The grid cells that form the sub-mask are then populated with their corresponding closest point data. The values in the inner sub-mask serve as Dirichlet boundary conditions for a less-accurate, but faster hyperbolic PDE-based extension method [33]. Here, to extend a quantity f, the following equation

$$\frac{\partial f}{\partial \hat{t}} + S(\psi) \frac{\nabla \psi}{|\nabla \psi|} \cdot \nabla f = 0$$

is solved iteratively in the outer mask where $S(\psi)$ is a smeared signum function on ψ. This is done so that the initialised signed-distance level set function ψ maintains its properties as the simulation progresses.

4. Analytical results

A premixed flame originating from an ignition source and freely propagating outwards into an infinitely large space (in two-dimensions) containing the combustible mixture is considered. Using polar coordinates, all variables are expressed in terms of the radial distance r and the polar angle θ. The hydrodynamic theory is valid once the flame attains a radius R_0 larger than the flame thickness, such that $\delta \equiv l_f / R_0 \ll 1$. Consequently, the propagating flame separates a pocket of burnt gas from the fresh unburnt mixture, as illustrated in Figure 4. If the state of the mixture, including pressure, density and temperature, are scaled with respect to their values in the fresh mixture, and R_0, S_L and R_0/S_L are used as representative length, speed and timescales, respectively, the problem can be recast in a dimensionless form comprising of Equations (1)– (4) with the flame speed relation expressed as $S_f = 1 - \delta\alpha\mathbb{K}$, where $\alpha = \mathcal{L}/l_f$ is the Markstein number. The only other parameter is the density ratio, or thermal expansion parameter $\sigma = \rho_u/\rho_b$, which is also equal to the temperature ratio T_b/T_u and hence proportional to the heat release. For future reference, the "reduced" Markstein number $\mathcal{M} = \mathcal{L}/R_0 = \delta\alpha$ is also defined and will be used in the numerical computations. Below, the same symbols will be used to express dimensionless variables.

Since $\delta \ll 1$, the solution of the expanding flame will be sought by expanding all variables in powers of δ.

4.1. *Basic state*

The basic state, corresponds to an outwardly propagating and symmetric circular flame given instantaneously by $r = R(t)$. The continuity equation implies that the pocket of burnt gas in $r < R(t)$ remains motionless, while the radial velocity u in unburnt gas, $r > R(t)$, is

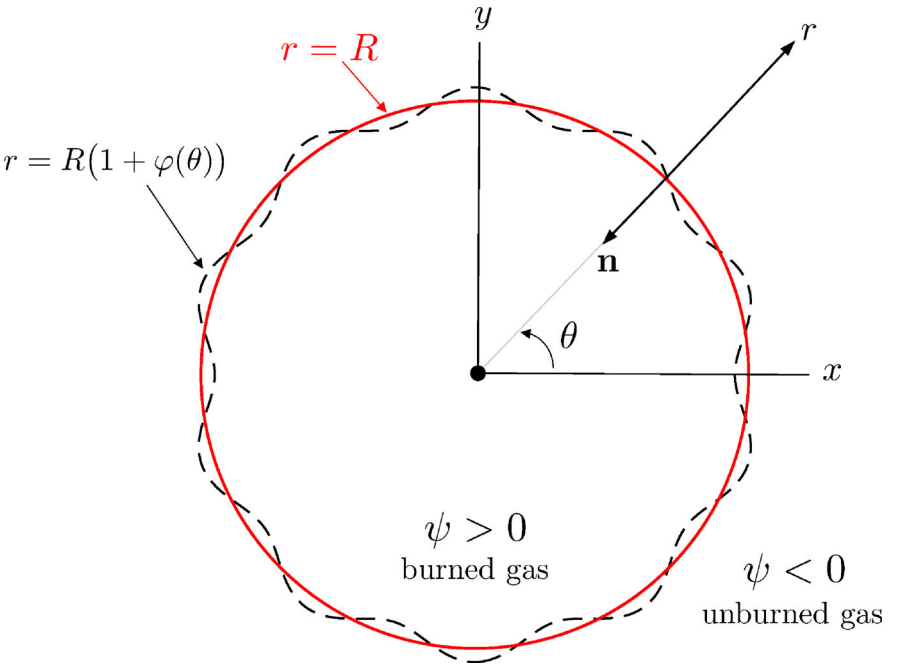

Figure 4. Schematic representation of a perturbed centrally ignited outgrowing flame; the flame surface is represented by $\psi(r,\theta) \equiv R[1+\varphi(\theta)] - r = 0$ (the dashed curve) with the unperturbed circular flame $r = R(t)$ shown as the solid curve (in red) (colour online).

inversely proportional to r. Mass conservation across the front and the flame speed relation then yield

$$u = \begin{cases} 0 & \text{for } r < R(t) \\ (\sigma-1)\left(1-\delta\,\dfrac{\sigma\alpha}{R}\right)\dfrac{R}{r} & \text{for } r > R(t) \end{cases}, \tag{14}$$

$$\frac{\mathrm{d}R}{\mathrm{d}t} = \sigma\left(1-\delta\,\frac{\sigma\alpha}{R}\right). \tag{15}$$

The stretch rate $\mathbb{K} = \sigma/R$, which results directly from (6), can be also expressed as a combination of curvature $\kappa = 1/R$ and strain $K_S = (\sigma-1)/R$, both of which diminish as the flame grows bigger. As a result, the expanding flame for mixtures that admit positive Markstein length experiences an increase in the propagation speed that tends towards a constant value proportional to the heat release. The effect of strain rate is to reduce the propagation speed, therefore increasing the time that it takes for the flame to (approximately) reach a steady rate.

Since $\partial p/\partial r = 0$ in the burnt gas region, the pressure in the enclosed region $r < R(t)$ varies in time but remains spatially independent. In the unburnt gas, $r > R(t)$, the momentum equation implies

$$\frac{\partial p}{\partial r} = -\frac{\mathrm{d}R}{\mathrm{d}t}\,\frac{\sigma-1}{r} + \left(1-2\delta\,\frac{\sigma\alpha}{R}\right)\frac{(\sigma-1)^2R^2}{r^3},$$

which can be integrated to determine the pressure field. The expression for $p(r,t)$ is not provided, as only the pressure gradient is required in the subsequent analysis.

Whilst the explicit expression

$$R = (1+\sigma t) - \delta\,\sigma\alpha\,\ln(1+\sigma t), \tag{16}$$

can be obtained by integrating Equation (15) for $\delta \ll 1$ with $R(0)=1$, the notation $R(t)$ will be used below to express the flame position with the understanding that it must be expanded in powers of δ, retaining terms correct to $\mathcal{O}(\delta)$ only.

4.2. *Linear stability analysis*

Since the basic state is continuously varying in time, stability or instability cannot be defined in the classical sense. Instead, instability is determined by the tendency of the flame to become continuously more distorted. Accordingly, if at a given instant the disturbance increases but the basic state grows more rapidly, the flame is considered momentarily stable since the disturbance relative to the flame front would appear decaying. On the other hand, if at a given instant the perturbation grows at a faster rate than the basic state, the flame is momentarily unstable. At the onset of instability, the perturbation starts growing at a rate faster than the underlying circular flame thereby resulting in a surface that becomes increasingly corrugated in time. It is therefore convenient to express the distorted flame front as

$$\psi \equiv R(t)\;[1+\varphi(\theta,t)] - r = 0, \tag{17}$$

such that the decay/growth of $\varphi(\theta,t)$, which represents the distortion of the flame front relative to the basic state, determines whether the flame is stable or not. The velocity and pressure fields are also decomposed accordingly

$$\mathbf{v} = \bar{\mathbf{v}}(r,t) + \mathbf{v}'(r,\theta,t), \quad p = \bar{p}(r,t) + p'(r,\theta,t),$$

where the "overbar" represents the unperturbed (basic) state whilst the "prime" identifies fluctuations about the mean. When introduced in Equations (1) and (2), and the resulting equations linearised about the basic state, one finds

$$\begin{aligned} &\nabla\cdot\mathbf{v}' = 0,\\ &\rho\left(\frac{\partial\mathbf{v}'}{\partial t} + (\bar{\mathbf{v}}\cdot\nabla)\mathbf{v}' + (\mathbf{v}'\cdot\nabla)\bar{\mathbf{v}}\right) = -\nabla p'\,. \end{aligned} \tag{18}$$

These equations must be solved subject to the jump conditions (4) across the perturbed interface (17) and the flame speed relation (5), appropriately linearised. In addition, $\mathbf{v}', p' \to 0$ as $r\to\infty$.

With the unit normal given by $\mathbf{n} \sim (-1,\ \varphi_\theta)$ and $u',\ v'$ denoting the velocity components in the r and θ directions, the velocities normal and tangential to the flame surface are $v_n = -\bar{u} - u'$ and $v_s = \bar{u}\,\varphi_\theta + v'$, respectively. The local curvature, propagation speed and stretch rate are

$$\begin{aligned} \kappa &\sim \frac{1}{R}(1-\varphi-\varphi_{\theta\theta}), \quad V_f \sim -R_t - (R\varphi)_t\\ \mathbb{K} &\sim \frac{R_t}{R} + \varphi_t - \frac{1}{R}\varphi_{\theta\theta} + \frac{1}{R}v'_\theta + \mathcal{O}(\delta) \end{aligned}$$

where subscripts with respect to the independent variables denote partial differentiation,

and use has been made of $\bar{u}^* - R_t \sim -1 + \mathcal{O}(\delta)$. The propagation speed and jump conditions may then be expressed at, and across the mean flame position $r = R(t)$, using a Taylor expansion, as follows:

At $\underline{r = R^+(t)}$

$$u' = (\sigma-1)\varphi + (R\varphi)_t + \frac{\delta\alpha}{R}\Big(-\sigma(\sigma-1)\varphi + R\varphi_t - \varphi_{\theta\theta} + v'_\theta\Big) \tag{19}$$

Across $\underline{r = R(t)}$

$$\begin{aligned}
[\![u']\!] &= -(\sigma-1)\varphi + \frac{\delta\alpha(\sigma-1)}{R}\Big(\sigma\varphi + R\varphi_t - \varphi_{\theta\theta} + v'_\theta\Big)\\
[\![v']\!] &= (\sigma-1)\varphi_\theta - \frac{\delta\alpha(\sigma-1)}{R}\,\sigma\varphi_\theta\\
[\![p']\!] &= -(\sigma-1)\varphi + \frac{2\delta\alpha(\sigma-1)}{R}\Big(-\tfrac{1}{2}\sigma(\sigma-2)\varphi + R\varphi_t - \varphi_{\theta\theta} + v'_\theta\Big).
\end{aligned} \tag{20}$$

The method of solving Equations (18) is different in each of the two regions. In the unburnt gas, the velocity field is irrotational and can therefore be expressed in terms of a velocity potential Φ, such that

$$\begin{aligned}
&\nabla^2\Phi = 0, \quad \mathbf{v}' = \nabla\Phi,\\
&\nabla\left(p' + \frac{\partial\Phi}{\partial t} + \bar{\mathbf{v}}\cdot\mathbf{v}'\right) = 0.
\end{aligned} \tag{21}$$

In the burnt gas, the flow is no longer potential. However, since $\bar{\mathbf{v}} = 0$, the perturbed equations reduce to

$$\begin{aligned}
&\rho\frac{\partial\mathbf{v}'}{\partial t} = -\nabla p', \quad \nabla^2 p' = 0,\\
&\nabla\cdot\mathbf{v}' = 0.
\end{aligned} \tag{22}$$

Decomposition into normal modes, yields

$$\begin{aligned}
u'(r,\theta,t) &= U(r,t)\,e^{in\theta}, \quad v'(r,\theta,t) = V(r,t)\,e^{in\theta},\\
p'(r,\theta,t) &= P(r,t)\,e^{in\theta}, \quad \varphi(\theta,t) = A(t)\,e^{in\theta},
\end{aligned}$$

where the integer n represents the perturbation wavenumber. For convenience, a rescaled time $T = (\sigma-1)t$ is introduced and, since conditions (19) and (20) are applied at a moving interface, the coordinate $x = r/R(T)$ is defined such that the position of the unperturbed flame is represented by $x = 1$ for all times. These transformations yield

$$\frac{\partial}{\partial r} = \frac{1}{R}\frac{\partial}{\partial x}, \quad \frac{\partial}{\partial t} = \sigma\frac{\partial}{\partial T} - \frac{\sigma\dot{R}}{R}x\frac{\partial}{\partial x}$$

where the "dot" signifies differentiation with respect to T. In the unburnt gas region ($x > 1$), Equations (21) become

$$\begin{aligned}
&x^2\frac{\partial^2\Phi}{\partial x^2} + x\frac{\partial\Phi}{\partial x} - n^2\Phi = 0\\
&U = \frac{1}{R}\frac{\partial\Phi}{\partial x}, \quad V = \frac{in}{R}\frac{\Phi}{x}, \quad P = -\sigma\left(\frac{\partial\Phi}{\partial T} - \frac{\dot{R}}{R}x\frac{\partial\Phi}{\partial x}\right) - \bar{u}\,U,
\end{aligned}$$

with

$$R \sim T - \delta\,\sigma\alpha \ln T, \quad \bar{u} \sim \left(1 - \delta\frac{\sigma\alpha}{T}\right)\frac{\sigma-1}{x}\,. \tag{23}$$

In the burnt gas region ($x < 1$), Equation (22) becomes

$$x^2\frac{\partial^2 P}{\partial x^2} + x\frac{\partial P}{\partial x} - n^2 P = 0$$
$$\frac{\partial U}{\partial T} - \frac{\dot{R}}{R}x\frac{\partial U}{\partial x} = -\frac{1}{R}\frac{\partial P}{\partial x}, \quad V = \frac{\mathrm{i}}{n}\frac{\partial (xU)}{\partial x}\,.$$

It is then a straightforward matter to integrate these equations in their respective regions, applying the conditions (19) and (20) at $x = 1$ along with the requirement that all perturbations decay far downstream.

All variables are expanded in powers of δ, namely in the form $U = U_0 + \delta U_1 + \cdots$, and solve recursively. To leading order, the solution in the unburnt gas region is

$$U_0 = -n\frac{B_0(T)}{T}x^{-(n+1)}, \quad V_0 = \mathrm{i}n\frac{B_0(T)}{T}x^{-(n+1)},$$
$$P_0 = -\sigma\left(\dot{B}_0(T) + \frac{nB_0(T)}{T}\right)x^{-n} + n(\sigma - 1)\frac{B_0(T)}{T}x^{-(n+2)}.$$

In the burnt gas region, the solution is

$$P_0 = C_0(T)\,x^n, \quad U_0 = -nG_0(T)x^{n-1} + D_0(xT),$$
$$V_0 = -\mathrm{i}nG_0(T)x^{n-1} + \frac{\mathrm{i}}{n}\frac{\partial (xD_0)}{\partial x}\,,$$

where $B_0 = B_0(T), G_0 = G_0(T), D_0 = D_0(xT)$ remain to be determined, and $C_0(T)$ results from

$$G_0(T) = T^{n-1}\int^T \tau^{-n}\,C_0(\tau)\,\mathrm{d}\tau\,.$$

The unknown functions B_0, D_0, G_0 and the amplitude of the flame-front perturbation A_0 are determined from the four conditions (19) and (20) which, to leading order, and after some algebraic manipulations[1] yield

$$\sigma T^2\frac{\mathrm{d}A_0}{\mathrm{d}T} + (2\sigma - 1)TA_0 + nB_0 = 0,$$
$$-\sigma T\frac{\mathrm{d}A_0}{\mathrm{d}T} - \sigma A_0 + D_0 - nG_0 = 0,$$
$$-(\sigma - 1)TA_0 - B_0 + \frac{T}{n^2}\frac{\mathrm{d}(TD_0)}{\mathrm{d}T} - TG_0(T) = 0,$$
$$(\sigma - 1)A_0 + \sigma\frac{\mathrm{d}B_0}{\mathrm{d}T} + \frac{n}{T}B_0 + T\frac{\mathrm{d}G_0}{\mathrm{d}T} - (n-1)G_0 = 0\,.$$

Since D_0 is a function of the product xT, the order of differentiation with respect to x and T are interchangeable, a property that has been used in deriving the above equations. The

system can be further reduced to a single differential equation for the amplitude A_0, namely

$$aT^2\frac{\mathrm{d}^2A_0}{\mathrm{d}T^2}+bT\frac{\mathrm{d}A_0}{\mathrm{d}T}+cA_0=0, \tag{24}$$

with

$$a=(\sigma+1)n,\quad b=2n^2+(2+4\sigma)n,$$
$$c=-[(\sigma-1)/\sigma]n^3+[(3\sigma-1)/\sigma]n^2+2\sigma n.$$

This equation admits solutions of the form T^ω where the exponent ω satisfies the quadratic equation $a\omega^2+(b-a)\omega+c=0$. Of the two roots, the one that corresponds to instability is

$$\omega=\frac{-(b-a)+\sqrt{(b-a)^2-4ac}}{2a}.$$

Up to a constant, that depends on the initial conditions at $T=1$, the remaining amplitudes are given by

$$A_0=T^\omega,\quad B_0=\beta_1T^{\omega+1},\quad D_0=\beta_2T^\omega,\quad G_0=\beta_3T^\omega,\quad C_0=\beta_4T^\omega,$$

with

$$\beta_1=(1-2\sigma-\sigma\omega)/n,\quad \beta_2=\sigma(\omega+1)+\beta_3\,n,$$
$$\beta_3=-[(\sigma-1)+(\sigma\omega+\sigma+n)\beta_1]/\beta_4,\quad \beta_4=(\omega+1)-n.$$

To $\mathcal{O}(\delta)$, the procedure is similar except that now the equations involve non-homogeneous terms arising from the expansion (23) of $R(T)$ and $\bar{u}(x,T)$. The solution in the unburnt gas region is

$$U_1=-n\left[\frac{B_1(T)}{T}+\alpha\sigma\beta_1\,T^{\omega-1}\ln T\right]x^{-(n+1)},$$
$$V_1=\mathrm{i}n\left[\frac{B_1(T)}{T}+\alpha\sigma\beta_1\,T^{\omega-1}\ln T\right]x^{-(n+1)},$$
$$P_1=-\dot{B}_1(T)\frac{\sigma}{x^n}+n\left[\frac{B_1}{T}+\alpha\sigma\beta_1(\ln T-1)T^{\omega-1}\right]\left[\frac{\sigma-1}{x^{n+2}}-\frac{\sigma}{x^n}\right],$$

and in the burnt gas region

$$P_1=C_1(T)\,x^n,$$
$$U_1=-nG_1(T)x^{n-1}+D_1(xT)+\alpha\sigma\left[\gamma_1x^{n-1}-(\gamma_2x^{n-1}+\gamma_3x^\omega)\ln T\right]T^{\omega-1},$$
$$V_1=-\mathrm{i}nG_1(T)x^{n-1}+\frac{\mathrm{i}}{n}\frac{\partial(xD_1)}{\partial x}+\mathrm{i}\alpha\sigma\left[\gamma_1x^{n-1}-(\gamma_2x^{n-1}+\gamma_4x^\omega)\ln T\right]T^{\omega-1},$$

with

$$G_1(T)=T^{n-1}\int^T\tau^{-n}\,C_1(\tau)d\tau$$

$$\gamma_1=\frac{n^2(\omega-n+1)}{(\omega-n)^2}\beta_3,\quad \gamma_2=\frac{n\omega}{\omega-n}\beta_3,\quad \gamma_3=\omega\beta_2,\quad \gamma_4=\frac{\omega+1}{n}\gamma_3\,,$$

where the unknown functions $B_1 = B_1(T)$, $G_1 = G_1(T)$, $D_1 = D_1(xT)$ remain to be determined. As before, B_1, G_1, D_1 and the correction to the amplitude A_1 are determined from the $\mathcal{O}(\delta)$ corrections of the four conditions (19) – (20). After some algebraic manipulations, one finds

$$\begin{aligned}
&\sigma T^2 \frac{\mathrm{d}A_1}{\mathrm{d}T} + (2\sigma - 1)TA_1 + nB_1 = \alpha\sigma\left[(J_1 + J_1' \ln T)T^{\omega}\right], \\
&-\sigma T \frac{\mathrm{d}A_1}{\mathrm{d}T} - \sigma A_1 + D_1 - nG_1 = \alpha\sigma\left[(J_2 + J_2' \ln T)T^{\omega-1}\right], \\
&-(\sigma - 1)TA_1 - B_1 + \frac{T}{n^2}\frac{\mathrm{d}(TD_1)}{\mathrm{d}T} - TG_1(T) = \alpha\sigma\left[(J_3 + J_3' \ln T)T^{\omega}\right], \\
&(\sigma - 1)A_1 + \sigma \frac{\mathrm{d}B_1}{\mathrm{d}T} + \frac{n}{T}B_1 + T\frac{\mathrm{d}G_1}{\mathrm{d}T} - (n-1)G_1 = \alpha\sigma\left[(J_4 + J_4' \ln T)T^{\omega-1}\right],
\end{aligned}$$

with

$$\begin{aligned}
J_1 &= 2\sigma - \omega - n^2(1-\beta_1)/\sigma - 1 \\
J_1' &= \sigma\omega - n\beta_1 \\
J_2 &= \sigma\omega - \sigma + n^2(1-\beta_1) - \gamma_1 \\
J_2' &= \gamma_2 + \gamma_3 - \sigma\omega \\
J_3 &= -\gamma_1/n - (\sigma - 1) \\
J_3' &= \gamma_2/n + \gamma_4/n + \beta_1 \\
J_4 &= [2n^2(1-\beta_1)/\sigma - \sigma + 2(\omega+1)](\sigma - 1) + n\beta_1 \\
J_4' &= -n\beta_1 .
\end{aligned}$$

This system can be reduced to a single non-homogeneous equation for A_1, namely

$$aT^2 \frac{\mathrm{d}^2 A_1}{\mathrm{d}T^2} + bT\frac{\mathrm{d}A_1}{\mathrm{d}T} + cA_1 = \alpha\sigma\,(H_1 + H_2 \ln T)\,T^{\omega-1} \tag{25}$$

with the differential operator identical to that in (24) and the constant H_1 and H_2 given by

$$\begin{aligned}
H_1 &= \frac{n}{\sigma}(\sigma\omega + 2n)J_1 + nJ_1' - \frac{n\omega}{\sigma}J_2 - \frac{nJ_2'}{\sigma} + \frac{n^3}{\sigma}J_3 - \frac{n^2}{\sigma}J_4, \\
H_2 &= \frac{n}{\sigma}(\sigma\omega + 2n)J_1' - \frac{n\omega}{\sigma}J_2' + \frac{n^3}{\sigma}J_3' - \frac{n^2}{\sigma}J_4' .
\end{aligned}$$

It can be verified that the particular solution of Equation (25) is

$$A_1 = \alpha\sigma\,(-\omega \ln T + Q)\,T^{\omega-1},$$

with

$$Q = \frac{\begin{array}{c} 2n^3 + [5\sigma + 2\omega(\sigma+1) - 3]n^2 \\ -\left(\sigma^2 - 2\sigma\omega^2 - 4\sigma\omega + 2\sigma + 2\omega - 1\right)n - \sigma\omega[\omega(\sigma-1) + 2\sigma] \end{array}}{2\,[(\sigma+1)\omega + n + \sigma]}.$$

Therefore, the amplitude of a disturbance with wavenumber n, scaled by its initial value, evolves in time according to

$$A(T) = T^{\omega}\left[1 + \delta\alpha\left(\frac{-\omega\sigma\ln T}{T} + \frac{Q}{T}\right) + \mathcal{O}(\delta^2)\right]. \tag{26}$$

Although similar expressions can be derived for the amplitude of the pressure and velocities, their exact form is not needed in the following discussion.

To isolate the influence that each of the two components of stretch, curvature and strain, exert on the flame stability, the entire analysis was repeated assuming that the flame speed relation (5) is replaced by $S_f = S_L(1 - \mathcal{L}\kappa)$. The results reveal that the evolution of disturbances is still represented by the expression (26), except now

$$Q = \frac{2n^3 + [(\sigma + 2\sigma\omega - 1)/\sigma]n^2 + [(4\sigma + 2\sigma\omega + \sigma^2 - 1)/\sigma]n - \omega[\omega(\sigma + 1) + 2\sigma]}{2[(\sigma + 1)\omega + n + \sigma]}.$$

Finally, it is noted that the linear stability results of the expanding circular flames presented above bear similarity to the results of spherically expanding flames [9, 10], but differ in the details; in particular the dependence of the expressions for ω and Q on n and σ.

4.3. *Growth rate*

Using R to now represent the *dimensional* mean radius of the perturbed flame as the independent variable, Equation (26) may be rewritten, correct to $\mathcal{O}(\delta)$, as

$$\frac{A}{A_0} = \left(\frac{R}{R_0}\right)^{\vartheta(R)}, \quad \vartheta = \omega + \frac{\mathcal{L}}{R}\,\frac{Q}{\ln(R/R_0)} \tag{27}$$

where A_0 here is the initial amplitude, and R_0 the initial flame size. To leading order, $A = A_0(R/R_0)^{\omega}$ and, for a perturbation of given wavenumber, the growth rate ω is modulated solely by the thermal expansion parameter σ. At a given instant, stability (and instability) depend on whether ω is negative (or positive). Figure 5 illustrates the marginal stability diagram which comprises a curve segregating the unstable region from the stable one. It demonstrates that in the absence of thermal expansion ($\sigma = 1$), all perturbations exhibit a negative growth-rate ($\omega < 0$). For finite values of thermal expansion ($\sigma > 1$); however, there exists a wavenumber n_0 above which the flame becomes unstable. The instability, which is due to gas expansion, is the well-known *hydrodynamic instability*. Indeed, in the limit of both, $n \gg 1$ and $R \gg R_0$ with $k = n/R$ fixed, which corresponds to a disturbance of wavenumber k (scaled with $1/R_0$) on a nominally curved, or nearly planar flame propagating at a speed $R \sim \sigma S_L t$, one finds that

$$\omega \sim \underbrace{\frac{-\sigma + \sqrt{\sigma^3 + \sigma^2 - \sigma}}{\sigma + 1}}_{\omega_{\mathrm{DL}}}\,\frac{kR}{\sigma};$$

such that $A \sim \exp(\omega_{\mathrm{DL}} k S_L t)$, which is the well-known Darrieus–Landau result.

The $\mathcal{O}(\delta)$ correction to the growth rate, contained in the second term of $\vartheta(R)$ proportional to the Markstein length $\mathcal{L}$, mimics the effects of thermal and molecular diffusion and

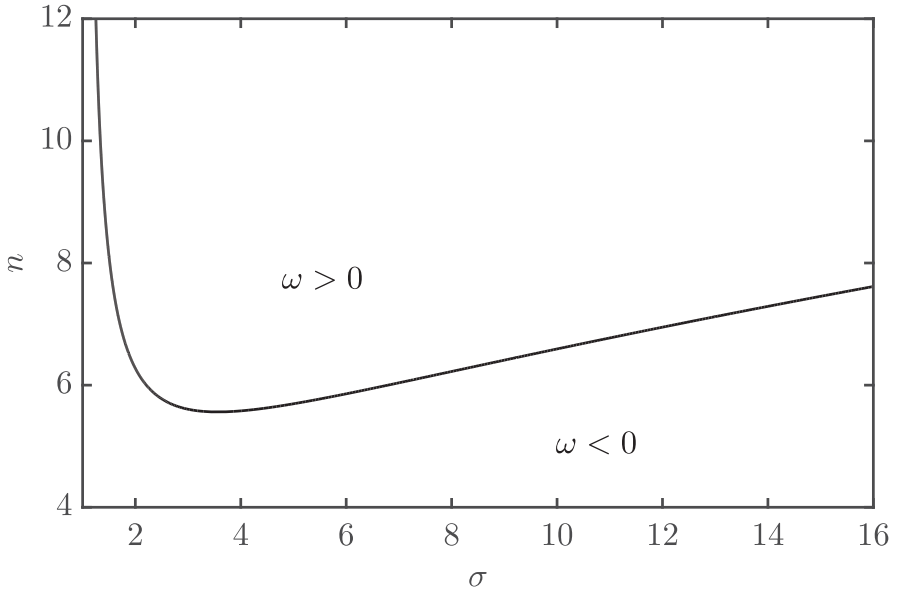

Figure 5. Neutral stability diagram showing regions of stability/instability based on the leading term of (26), or the asymptotic limit $\delta \to 0$.

is significant only during the early stages of propagation. Its effect becomes gradually less important when the flame grows bigger and has a negligible influence when $\mathcal{L}/R \to 0$; a limit in which the flame is hydrodynamically unstable. The growth/decay in amplitude of a disturbance of wavenumber n given by

$$\frac{1}{A}\frac{\mathrm{d}A}{\mathrm{d}R} = \frac{1}{R}\left(\omega - \frac{\mathcal{L}}{R}Q\right) \tag{28}$$

shows that for mixtures with $\mathcal{L} > 0$, the flame surface initially grows faster than disturbances evolve on its surface. Thermo-diffusive effects exert a stabilising influence on all disturbances, which are limited to relatively short wavelength bounded by the flame circumference. When $R > (Q/\omega)\mathcal{L}$, on the other hand, the expanding flame is unable to suppress the growth of the disturbances due to hydrodynamic effects and the flame becomes unstable. For mixtures with $\mathcal{L} < 0$, thermo-diffusive effects have a destabilising influence and disturbances on the flame surface grow immediately upon their inception; possible stabilising effects could occur when the flame size is on the order of the flame thickness (or $R \ll R_0$), a limit not considered here. Indeed, experiments involving propagating spherical flames have shown that in mixtures deficient in the less mobile reactant, such as the fuel in lean (heavy) hydrocarbon-air or the oxidiser in rich hydrogen-air mixtures, the flame surface acquires a corrugated appearance only once it grows to a certain size. It is noted parenthetically that, in contrast to molecular and thermal diffusion, viscous effects (neglected in this study), play a secondary role on flame stability [4, 6]; they exert a stabilising influence, when variation in the mixture viscosity across the flame is accounted for [11, 34].

Figure 6 graphs the time history of the amplitude A as a function of flame size R obtained from Equation (27) for perturbations with different wavenumbers n, for a mixture with

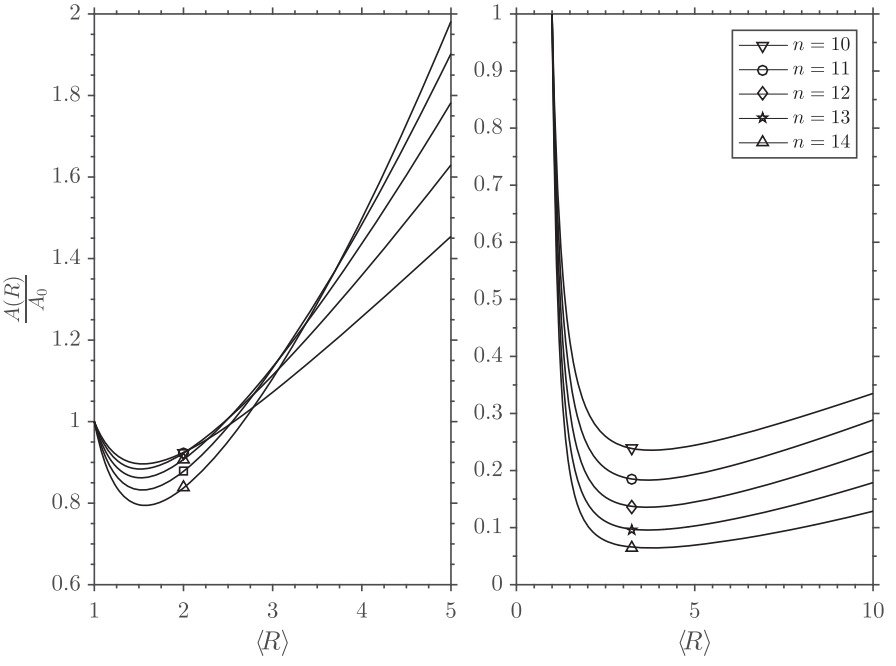

Figure 6. Variation in normalised amplitude A as a function of flame size as predicted by linear theory for a range of wavenumbers n in the absence (left figure) and presence (right figure) of strain-rate effects; the unburnt mixture into which the flame is propagating is characterised by $\mathcal{M} = 0.03$ and $\sigma = 5$.

$\sigma = 5$ and $\mathcal{M} = \mathcal{L}/R_0 = 0.03$. The left figure is based on the hypothetical case in which the flame speed depends only on curvature with hydrodynamic strain not affecting the propagation; the right figure corresponds to the case in which the flame speed depends on the stretch rate that includes both curvature and strain effects. In both cases, the evolution of the different perturbations is qualitatively similar. The amplitude of each perturbation decays initially during a period where curvature/stretch effects are significant with the initial rate of decay of larger wavenumber perturbations being greater owing to a large number of corrugations on the flame surface. This translates to larger peak curvatures and, by extension, stretch rates. As the flame becomes progressively larger, the stabilising influence of stretch diminishes and beyond a certain radius, the perturbations begin to grow. The graphs further demonstrate that the inclusion of strain further suppresses these disturbances and delays the point at which they begin to grow, consistent with the results in [35] for planar flames. Upon closer inspection, it is also seen that there exists a disturbance, characterised by wavenumber n_c, which is the first to grow. The corresponding flame radius, henceforth referred to as the critical radius, at which this disturbance begins to grow marks the onset of the instability.

The thermo-diffusive influence on flame stability, which play a crucial role in stabilising the short wavelength disturbances for $\mathcal{L} > 0$ is consistent with the stability results of planar flames. Once again, by considering the limit of both, $n \gg 1$ and $R \gg R_0$ with $k = n/R$ fixed,

$$Q \sim \frac{(\sigma + \omega_{\text{DL}})(1 + \omega_{\text{DL}})}{\sigma + (\sigma + 1)\omega_{\text{DL}}} k^2 R^2$$

and, since for such a large flame $R \sim \sigma t$, Equation (27) simplifies to

$$A \sim \exp\left[\omega_{\text{DL}} k - \mathcal{L}\,\frac{\sigma(\sigma+\omega_{\text{DL}})(1+\omega_{\text{DL}})}{\sigma+(\sigma+1)\omega_{\text{DL}}}\,k^2\right] S_L t$$

similar to the stability result of a planar flame [35]; see also [23].

Similar to the stability results attained for spherically expanding flames [10], curves of marginal stability are obtained by setting the right-hand side in (28) equal to zero, such that

$$\text{Pe} = \frac{\mathcal{L}}{l_f}\,\frac{Q(\sigma, n)}{\omega(n)}$$

where $\text{Pe} = R/l_f = RS_L/\mathcal{D}_{th}$ is the Péclet number. For a given σ, the curve traces a peninsula-like shape in the $n-Pe$ plane, with the nose determining the critical flame size and wavenumber at the onset of instability. The region enclosed by the peninsula identifies the range of unstable modes $n_{\min} < n < n_{\max}$ for a given flame radius R. Disturbances with wavelength larger than $2\pi R/n_{\min}$ are stabilised by stretch, whereas disturbances with wavelength shorter than $2\pi R/n_{\max}$ are stabilised by the influences of diffusion. It can be verified that the upper branch of the marginal curve asymptotes to the line $R = \mathcal{L}\Gamma\, n^*_{\max}$, where Γ is a constant that depends only on σ, whilst the lower branch asymptotes to the line $n = n^*_{\min}$ where $n^*_{\min}$ is a constant that depends only on σ. Hence, for a given mixture (fixed σ), the smallest possible cell size, $\lambda_{\min} = 2\pi R/n^*_{\max} = 2\pi\mathcal{L}\,\Gamma$, is a constant, whilst the largest possible cell size, $\lambda_{\max} = 2\pi R/n^*_{\min} = (2\pi/n^*_{\min})R$, increases linearly as the flame expands, and may split eventually into smaller cells. This development, however, cannot be predicted by linear theory and will be discussed in a subsequent paper. Curves of neutral stability are graphed below; see, for example, Figures 10 and 11 in the numerical results section.

5. Numerical Results

A flame kernel with an initial radius of 1 is initialised at the centre of a square domain of length $L = 48$. Through numerical experimentation, this was deemed large enough to ensure that boundary effects did not pollute the solution. All reported simulations are performed at a grid resolution of 128 points per unit length. Realistic zero-Neumann boundary conditions are prescribed for ψ and $\mathbf{v}$ whilst the pressure is set equal to zero hence simulating an open, constant pressure domain.

5.1. *Unperturbed flame*

In the absence of disturbances, the expanding circular flame propagates smoothly for all time $t > 0$, as shown in Figure 7. The graph illustrates the variation in propagation speed $d\langle R\rangle/dt$ as a function of flame position in the absence (top panel) and presence (bottom panel) of strain-rate effects, for different values of the thermal expansion parameter. In anticipation of deformations to the circular flame surface, $\langle R\rangle = L/(2\pi)$ is defined to represent an effective flame radius where L is the flame length or perimeter. As the flame's radius becomes large, the effects of flame stretch diminish and the propagation speed tends to the asymptotic value $dR/dt \sim \sigma$ predicted by the theory. The incorporation of strain-rate effects (solid lines), inhibits the acceleration experienced by the flame-front, an aspect that will become pertinent in later discussions.

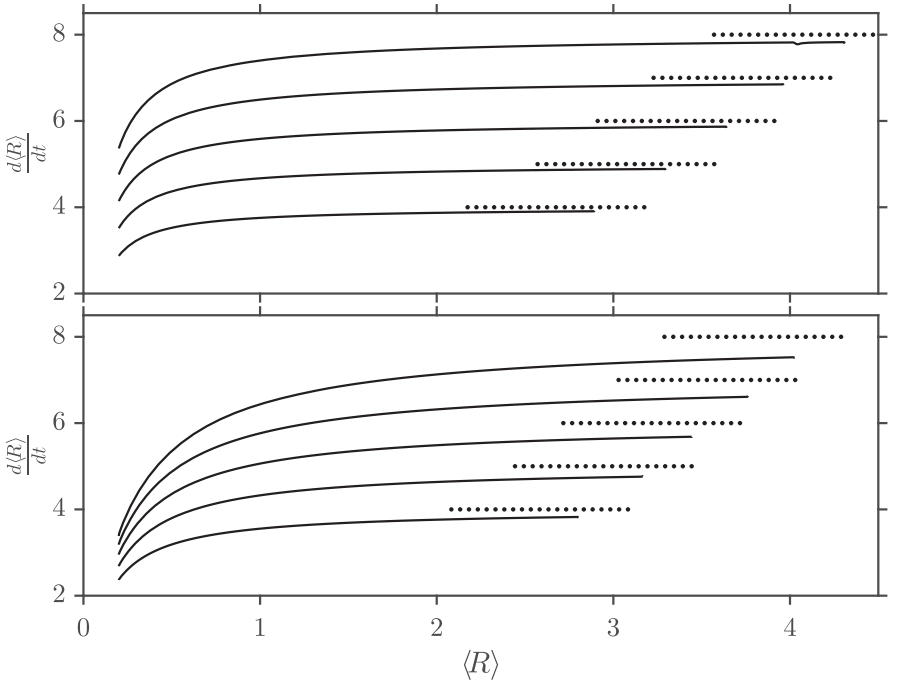

Figure 7. The propagation speed as a function of flame position in the absence (top panel) and presence (bottom panel) of strain-rate effects, for thermal expansion parameter values $\sigma = 4, 5, 6, 7, 8$ and $\mathcal{M} = 0.04$; the asymptotic behaviour $dR/dt \sim \sigma$ is shown by the dotted line.

5.2. *Flame wrinkling*

This predicted behaviour shown in Figure 6 is corroborated numerically by perturbing the initial kernel with the form $r = 1 + A_0 \cos n\theta$ with $A_0 = 10^{-3}$ and $n \in [9,\ 19]$. The flame, in each case, is then allowed to propagate freely. At each instant, the perturbations on the flame surface are computed and normalised as follows

$$A^* = \frac{R - \langle R\rangle}{\langle R\rangle}.$$

A discrete Fast Fourier transform (DFFT) of this signal is taken and the amplitude of the disturbance corresponding to n is measured.

The outcome is illustrated in Figures 8 and 9, where the former corresponds to flame propagation at a speed that depends solely on curvature (neglecting the influences of strain-rate) and the latter where the flame speed depends on the stretch rate, which includes both curvature and strain-rate. The left panel of Figure 8, which depicts the variation in the normalised amplitudes growth rates with respect to the effective flame radius, is in agreement with the outcome of linear theory. The relative amplitude of each perturbation initially decays, with larger wavenumber perturbations decaying more rapidly. At some finite radius, the growth rates approach a minimum beyond which the relative amplitude of perturbation begins to grow. As alluded to previously, each perturbation reaches a minimum at a different flame radius. The perturbation with wavenumber n_c which is first to grow, determines the critical radius R_c that marks the onset of instability. This is shown in

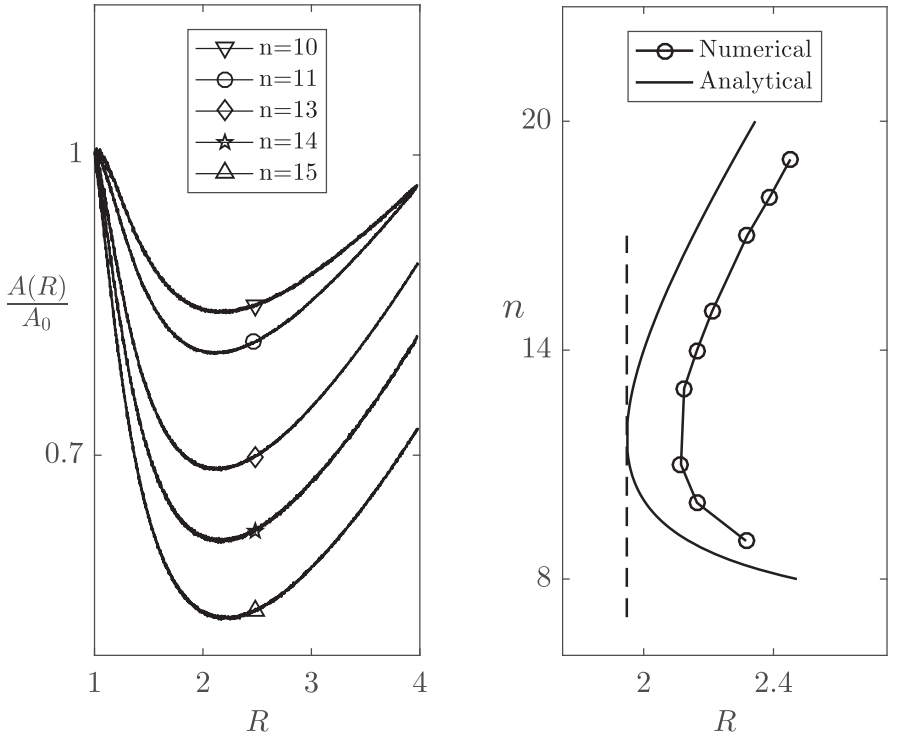

Figure 8. Stability results of an outgrowing flame propagating at a speed that depends solely on curvature (strain-rate effects neglected), for mixtures with $\mathcal{M} = 0.04$ and $\sigma = 6$. The left panel corresponds to the normalised growth rate, computed numerically, of various integer wavenumber disturbances as a function of the flame size; the right panel displays a comparison of the numerically computed values of the wavenumber at the onset of instability with the linear theory results.

the panel on the right, which graphs (circles) for each disturbance the flame position where the growth rate attains its minimum value, or the marginally stable states. The nose of this peninsula-like curve corresponds to the critical flame size R_c and wavenumber n_c. Superimposed alongside the numerical results is the marginal stability curve derived from linear theory. The results display an overall good quantitative agreement; the minimal offset is attributed to the fact that in the numerical implementation, the flame is not infinitesimally thin but is diffused over a few grid points. While a reduction in the numerical flame thickness translates this curve closer to the analytical result, it results in undesirable numerical artefacts. It should be noted that if the initial amplitude is halved or doubled, the same growth rate is obtained which is consistent with the linear theory results.

The evolution of these disturbances when effects of strain-rate are accounted for is graphed in Figure 9. The behaviour is qualitatively similar to the preceding discussion and good quantitative agreement with linear theory is demonstrated. More significantly, it shows that despite the smaller Markstein number selected ($\mathcal{M} = 0.02$ instead of 0.04), which reduces the stabilising influence exerted by thermo-diffusive effects, the incorporation of strain-rate effects in the flame speed expression dampens the growth-rate of the perturbations thereby allowing the flame to remain stable up to a larger radius. The substantial role that strain-rate effects play in delaying the onset of instability, absent in earlier

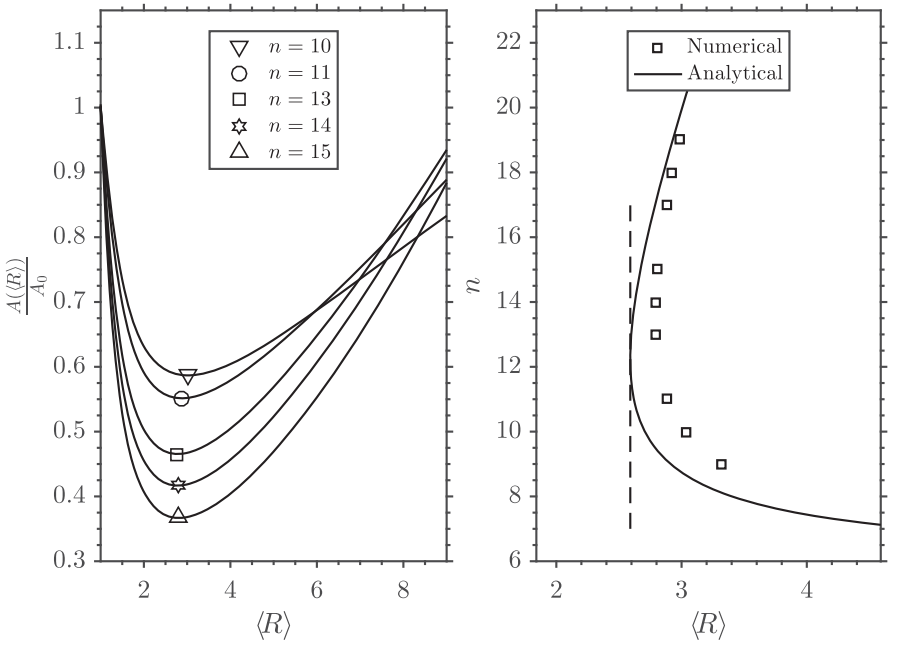

Figure 9. Stability results of an outgrowing flame propagating at a speed that depends on flame stretch, namely when both curvature and strain-rate effects are considered, for mixtures with $\mathcal{M} = 0.02$ and $\sigma = 6$; the left and right panels display similar plots as in Figure 8.

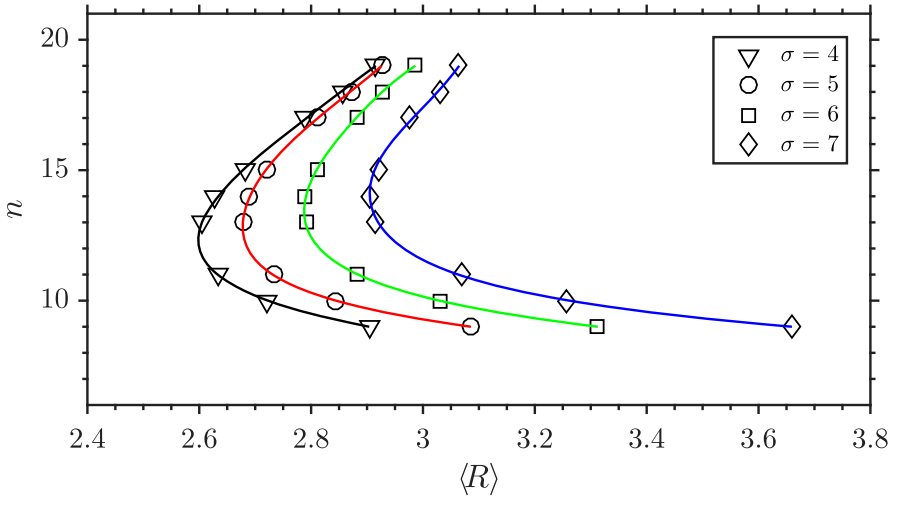

Figure 10. The marginal stability peninsula for increasing values of the thermal expansion parameter σ, for a fixed Markstein number $\mathcal{M} = 0.02$ (colour online).

numerical studies [36–38], has not been previously recognised. The former two works are based on weakly nonlinear Sivashinsky type equations derived in the limit of small thermal expansion ratios whilst the latter uses a simplified flame speed relation which omits the straining effects of the underlying flow field.

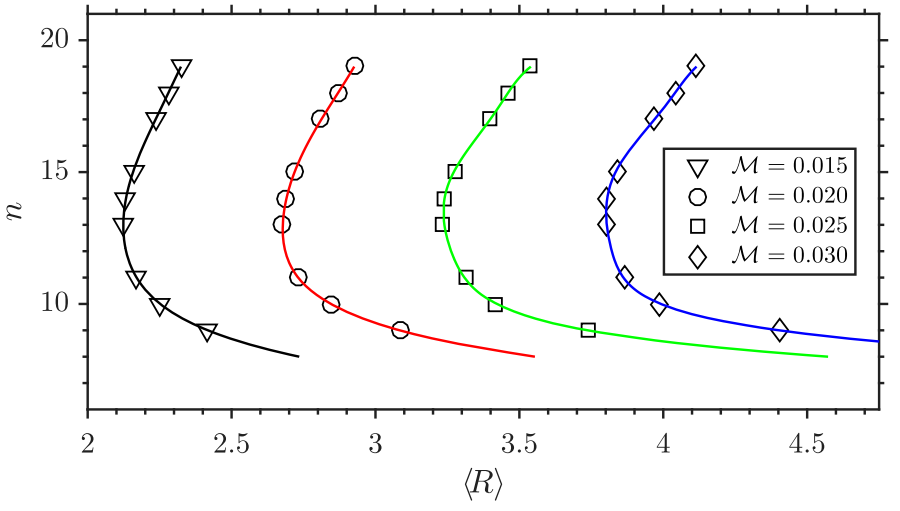

Figure 11. The marginal stability peninsula for increasing values the increasing Markstein number $\mathcal{M}$, for a fixed value of $\sigma = 5$ (colour online).

Having established the marked influence of strain in further stabilising the expanding flame, the effect of varying the thermal expansion parameter, whilst maintaining the Markstein number is illustrated in Figure 10. As σ increases, the nose of the peninsula shifts towards the right indicating a delay in the onset of instability. This is attributed to the fact that larger gas expansion, or heat release, causes the underlying flame to propagate relatively faster than the superimposed disturbances leading to an increasingly smoother surface for a greater duration. Additionally, there is a subtle increase in n_c. Similarly, Figure 11 depicts the marginal stability peninsula for four distinct Markstein numbers maintaining the same thermal expansion parameter ($\sigma = 5$). It can be seen that as $\mathcal{M}$ increases, the peninsula translates further to the right. This is explained by the increased thermal and molecular diffusion brought about by the increased Lewis number. Equivalently, it can be interpreted as an increase in flame thickness δ (recall $\mathcal{M} = \delta\mathcal{L}$) which also leads to greater stability.

Since disturbances in actuality are irregular, the evolution of an initially imposed polychromatic disturbance is examined. Such disturbances may be expressed in the form

$$r = 1 + \sum_k A_k \cos(n_k\theta + \psi_k)$$

where the phases ψ_k are chosen randomly in the interval $[0,\ \pi]$, with small amplitudes A_k. For the subsequent experiment, $k = 6$ was selected with disturbances of wavenumbers $n = [9,\ 19]$, phases $\psi = [0.23,\ 0.017,\ 1.09,\ 1.08,\ 0.68,\ 0.42]$ and amplitudes $A = [2.0,\ 1.57,\ 1.97,\ 1.75,\ 1.37,\ 1.48] \times 10^{-3}$. As before, the flame is allowed to evolve freely and the evolution of different wavenumbers are tracked; the results of which are graphed in Figure 12. For comparison, the turning points for monochromatic perturbations are superimposed on the graph under identical conditions i.e. $\mathcal{M} = 0.02$ and $\sigma = 5$. Despite the simultaneous presence of perturbations with varying wavenumbers and differing amplitudes, the growth rates are not affected. This is shown in the lack of alteration of the turning points when compared to monochromatic disturbances. It demonstrates that,

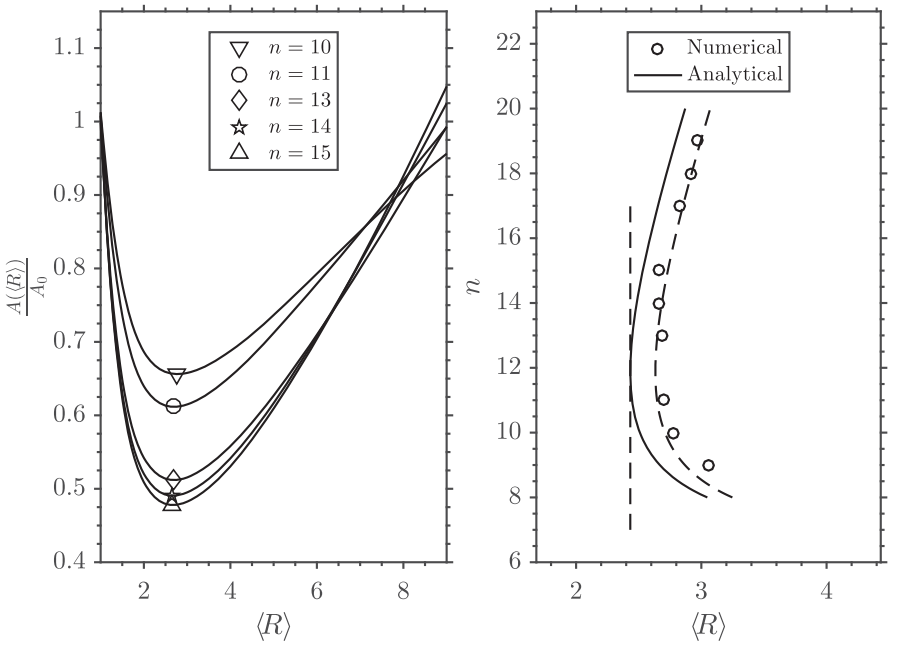

Figure 12. Stability results of an outgrowing flame subject to an initially imposed polychromatic disturbance, for mixtures with $\mathcal{M} = 0.02$ and $\sigma = 6$; the left and right panels display similar plots as in Figure 8 (colour online).

at least while the amplitude of the disturbances is small, the wavenumber interaction is negligible and that linear theory is still valid.

6. Conclusions

The embedded-manifold/Navier–Stokes methodology developed in this paper to address the nonlinear free-boundary hydrodynamic problem, obtained in the asymptotic limit in which the flame thickness is small compared to all other length scales, is a significant improvement of earlier versions. The refinements include (i) the application of a high-order geometrical closest point method to propagate surface quantities that are strictly defined on the flame surface onto the Cartesian grid used to solve the flow field; (ii) a high-order (fifth-order in this study) polynomial approximation of the interface to evaluate the unit vector normal to the flame surface and its gradients, as well as the local curvature; (iii) a stable interpolation technique to evaluate flow quantities at the Lagrangian mesh distributed along the flame interface. The method, applied to outgrowing flames (in two-dimensions) was shown to be efficient and robust, capturing with sufficient accuracy analytical results, including the long time propagation of symmetric smooth flames, the onset of the hydrodynamic instability and the early development of the cellular flame.

The analytical results and the supporting computational study have conclusively demonstrated that in the linear regime, where stretch has a tangible effect and the Lewis number of the mixture is above criticality, the relative amplitude of the perturbations initially undergo a sustained period of decay wherein the flame surface becomes progressively smoother before becoming cellular. The critical radius at which this transition occurs is shown to

be a function of the physicochemical parameters of the mixture, increasing with the thermal expansion and Markstein number. The substantial role that strain-rate effects play in delaying the onset of instability is demonstrated.

Experimental results which have examined the propagation of spherical flames have shown that a flame only adopts a cellular appearance at a radii larger than that predicted by linear theory. The onset was similarly noted in the present simulations to occur at a larger flame radius. This indicates that both phenomena are observed when the relative amplitude reaches a size much larger than its initial magnitude. While variable transport properties have been attributed to the underestimation of the critical radius [10], a more fundamental reason for the delay is that the disturbance preserves it co-sinusoidal distribution for a significant duration after the critical radius.

Note

1. The details can be found in [39] and will be omitted. Note, however, there are several typos in the thesis which have been corrected here. The interested reader should also consult the equivalent discussion on spherical flames presented in [9].

Disclosure statement

No potential conflict of interest was reported by the author(s).

Funding

This work was supported by Division of Chemical, Bioengineering, Environmental, and Transport Systems [ACI-1238993, CBET 19-11530, OCI-0725070]. This work has been partially supported by the CBET division of the National Science Foundation [grant number 19-11530]. This research is part of the Blue Waters sustained-petascale computing project, which is supported by the National Science Foundation (awards OCI-0725070 and ACI-1238993) the State of Illinois, and as of December, 2019, the National Geospatial-Intelligence Agency. Blue Waters is a joint effort of the University of Illinois at Urbana-Champaign and its National Center for Supercomputing Applications. It was also supported by the DOD High Performance Computing , subproject AFOSR42652011. The authors are indebted to C. Pantano–Rubino for helpful discussions concerning the application of the closest point method.

ORCID

Shikhar Mohan http://orcid.org/0000-0001-7339-8505

References

[1] G. Darrieus, *Propagation d'un front de flamme*. Unpublished work. Presented at La Technique Moderne (Paris) and in 1945 at Congrès de Mécanique Appliquée (Paris), 1938.
[2] L. Landau, On the theory of slow combustion, Dyn. Curved Fronts XIX(1) (1944), pp. 403–411.
[3] G.H. Markstein, Experimental and theoretical studies of flame-front stability, J. Aeronaut. Sci. 18 (1951), pp. 199–209.
[4] P. Pelce and P. Clavin, Influence of hydrodynamics and diffusion upon the stability limits of laminar premixed flames, J. Fluid. Mech. 124 (1982), pp. 219–237.
[5] M.L. Frankel and G.I. Sivashinsky, The effect of viscosity on hydrodynamic stability of a plane flame front, Combust. Sci. Technol. 29 (1982), pp. 207–224.
[6] M. Matalon and B.J. Matkowsky, Flames as gasdynamic discontinuities, J. Fluid. Mech. 124 (1982), pp. 239–259.

[7] M. Matalon and B. Matkowsky, Flames in fluids their interactions and stability, Combust. Sci. Technol. 34 (1983), pp. 295–316.
[8] A.G. Istratov and V.B. Librovich, On the stability of gasdynamic discontinuities associated with chemical reactions. The case of a spherical flame, Astronautica Acta 14 (1969), pp. 453–467.
[9] J. Bechtold and M. Matalon, Hydrodynamic and diffusion effects on the stability of spherically expanding flames, Combust. Flame. 67 (1987), pp. 77–90.
[10] R. Addabbo, J.K. Bechtold, and M. Matalon, Wrinkling of spherically expanding flames, Proc. Combust. Instit. 29 (2002), pp. 1527–1535.
[11] M. Matalon, C. Cui, and J. Bechtold, Hydrodynamic theory of premixed flames: Effects of stoichiometry, variable transport coefficients and arbitrary reaction order, J. Fluid Mech. 487 (2003), pp. 179–210.
[12] E.G. Groff, The cellular nature of confined spherical propane-air flames, Combust. Flame. 48 (1982), pp. 51–62.
[13] D. Bradley and C.M. Harper, The development of instabilities in laminar explosion flames, Combust. Flame. 99 (1994), pp. 562–572.
[14] S. Tse, D. Zhu, and C. Law, Morphology and burning fluxes of expanding spherical flames in H2/O2/inert mixtures up to 60 atmospheres, Proc. Combust. Inst. 28 (2000), pp. 1793–1800.
[15] O. Kwon, G. Rozenchan, and C. Law, Cellular instabilities and self-acceleration of outwardly propagating spherical flames, Proc. Combust. Inst. 29 (2002), pp. 1775–1783.
[16] C. Law, G. Jomaas, and J. Bechtold, Cellular instabilities of expanding hydrogen/propane spherical flames at elevated pressures: Theory and experiment, Proc. Combust. Inst. 30 (2005), pp. 159–167.
[17] G. Jomaas, C.K. Law, and J.K. Bechtold, On transition to cellularity in expanding spherical flames, J. Fluid. Mech. 583 (2007), pp. 1.
[18] J. Beeckmann, R. Hesse, S. Kruse, A. Berens, N. Peters, H. Pitsch, and M. Matalon, Propagation speed and stability of spherically expanding hydrogen/air flames: Experimental study and asymptotics, Proc. Combust. Insti. 36 (2017), pp. 1531–1538.
[19] Y. Rastigejev and M. Matalon, Numerical simulation of flames as gasdynamic discontinuities, Combust. Theory Modell. 10 (2006), pp. 459–481.
[20] F. Creta and M. Matalon, Propagation of wrinkled turbulent flames in the context of hydrodynamic theory, J. Fluid. Mech. 680 (2011), pp. 225–264.
[21] N. Fogla, F. Creta, and M. Matalon, Effect of folds and pockets on the topology and propagation of premixed turbulent flames, Combust. Flame 162 (2015), pp. 2758–2777.
[22] A. Patyal and M. Matalon, Nonlinear development of hydrodynamically-unstable flames in three-dimensional laminar flows, Combust. Flame 195 (2018), pp. 128–139.
[23] M. Matalon, The Darrieus–Landau instability of premixed flames, Fluid. Dyn. Res. 50 (2018), pp. 051412.
[24] M. Matalon, On flame stretch, Combust. Sci. Technol. 31 (1983), pp. 169–181.
[25] G.K. Giannakopoulos, C.E. Frouzakis, S. Mohan, A.G. Tomboulides, and M. Matalon, Consumption and displacement speeds of stretched premixed flames – theory and simulations, Combust. Flame. 208 (2019), pp. 164–181.
[26] Y. Rastigejev and M. Matalon, Nonlinear evolution of hydrodynamically unstable premixed flames, J. Fluid. Mech. 554 (2006), pp. 371–392.
[27] A.S. Almgren, J.B. Bell, P. Colella, L.H. Howell, and M.L. Welcome, A conservative adaptive projection method for the variable density incompressible Navier–Stokes equations, J. Comput. Phys. 142 (1998), pp. 1–46.
[28] C.S. Jiang and C.W. Shu, Efficient implementation of weighted ENO schemes, J. Comput. Phys. 126 (1996), pp. 202–228.
[29] R. Fedkiw, T. Aslam, B. Merriman, and S. Osher, A non-oscillatory Eulerian approach to interfaces in multimaterial flows (the ghost fluid method), J. Comput. Phys. 152 (1999), pp. 457–492.
[30] M. Bertalmío, L.T. Cheng, S. Osher, and G. Sapiro, Variational problems and partial differential equations on implicit surfaces, J. Comput. Phys. 174 (2001), pp. 759–780.
[31] C.B. MacDonald and S.J. Ruuth, Level set equations on surfaces via the closest point method, J. Sci. Comput. 35 (2008), pp. 219–240.
[32] R.I. Saye, High-order methods for computing distances to implicitly defined surfaces, Comm. App. Math. Comp. Sci. 9 (2014), pp. 107–141.

[33] D. Peng, B. Merriman, S. Osher, H. Zhao, and M. Kang, A PDE-based fast local level set method, J. Comput. Phys. 155 (1999), pp. 410–438.
[34] P. Clavin and P. Garcia, The influence of the temperature dependence of diffusivities on the dynamics of flame fronts., Journale De Mecanique Theorique Et Appliquee 2 (1983), pp. 245–263.
[35] F. Creta and M. Matalon, Strain rate effects on the nonlinear development of hydrodynamically unstable flames, Proc. Combust. Inst. 33 (2011), pp. 1087–1094.
[36] L. Filyand, G.I. Sivashinsky, and M.L. Frankel, On self-acceleration of outward propagating wrinkled flames, Phys. D: Nonlinear Phenomena 72 (1994), pp. 110–118.
[37] M. Rahibe, N. Aubry, G.I. Sivashinsky, and R. Lima, Formation of wrinkles in outwardly propagating flames, Phys. Rev. E. 52 (1995), pp. 3675–3686.
[38] K.L. Pan and R.V. Fursenko, Characteristics of cylindrical flame acceleration in outward expansion, Phys. Fluids 20 (2008), pp. 094107.
[39] S. Mohan, *Nonlinear development of centrally ignited expanding flames in laminar and turbulent mediums*, Ph.D. thesis, University of Illinois at Urbana-Champaign, 2020.